Scientific Research Publishing

International Journal of Geosciences, 2024, 15, 737-763
https://www.scirp.org/journal/ijg
ISSN Online: 2156-8367
ISSN Print: 2156-8359

A Dynamic Coupling of Ocean and Plate Motion

Yongfeng Yang

Water Resources Comprehensive Development Center, Bureau of Water Resources of Shandong Province, Jinan, China
Email: roufeng_yang@outlook.com

How to cite this paper: Yang, Y.F. (2024) A Dynamic Coupling of Ocean and Plate Motion. *International Journal of Geosciences*, **15**, 737-763.
https://doi.org/10.4236/ijg.2024.159041

Received: September 5, 2024
Accepted: September 23, 2024
Published: September 26, 2024

Abstract

Plate motion representing a remarkable Earth process is widely attributed to several primary forces such as ridge push and slab pull. Recently, we have presented that the ocean water pressure against the wall of continents may generate enormous force on continents. Continents are physically fixed on the top of the lithosphere that has been already broken into individual plates, this attachment enables the force to be laterally transferred to the lithospheric plates. In this study, we combine the force and the existing plate driving forces (*i.e.*, ridge push, slab pull, collisional, and shearing) to account for plate motion. We show that the modelled movements for the South American, African, North American, Eurasian, Australian, Pacific plates are well agreement with the observed movements in both speed and azimuth, with a Root Mean Square Error (RMSE) of the modelled speed against the observed speed of 0.91, 3.76, 2.77, 2.31, 7.43, and 1.95 mm/yr, respectively.

Keywords

Ocean Water Pressure Force, Ocean-Continent Interaction, Plate Driving Force, Lithospheric Plate, Plate Motion

1. Introduction

One of the most significant achievements in the 20th century was the establishment of plate tectonics, which developed from the previous concept of continental drift [1] [2]. Plate tectonics mainly describes the motion of a dozen different-sized plates that connect with each other to form a giant "jigsaw puzzle" over the Earth's surface. The evidence supporting this motion includes shape fitting of the African and American continents, a coal belt crossing from North America to Eurasia, identical directions of ice sheet movement in southern Africa and India, and Global Positioning System (GPS) speed measurements. In addition, paleomagnetic reversals in oceans [3] [4] reflect seafloor spreading, and studies of the Hawaii-Emperor seamount chain have shown that the chain is actually a trace of the

lithosphere rapidly moving over relatively motionless hotspots [5] [6], which further confirms the Earth's surface motion. During the past 50 years, our understanding of plate motion has expanded greatly. Plates were found to have been periodically dispersed and aggregated in the Mesozoic period, accompanied by 5 - 6 significant astronomical events [7]-[11]. The speed and direction of plate motion supported by paleomagnetism and deformation in the intraplate regions exhibited various styles over geological time [12].

Exploring the plate driving forces is especially important because it provides the first insights into the processes that yield plate tectonics. Throughout the history of plate tectonics, a large number of forces (*i.e.*, centrifugal and tidal forces, ridge push, slab pull, basal drag, slab suction, mantle plume, geoid deformation, and the Coriolis force) have been presented to account for plate motion [1] [5] [13]-[31]. More than 71% of the Earth's surface is covered by oceans, and their depths reach nearly 3700 meters [32]. Based on the principle of fluid mechanism that the water pressure against the wall of a container may generate force on the container, the ocean water pressure may generate enormous force on continents. Continents are physically fixed on the top of the lithosphere that has been already broken into individual plates, this attachment enables the force to be transferred laterally to the lithospheric plates. Recently, we have determined the distribution of this force around continents, and estimated its amplitude to be of the order of 10^{17} N per kilometer of continent width [33]. Our modelling suggested that the stresses yielded by this force are mostly concentrated on the upper part of the continental crust, and their magnitudes reach up to 2.0 - 6.0 MPa, which is entirely comparable to the range of earthquake stress drops (1 - 30 MPa) [34]. As a result, this force may have significantly impacted continents during a geological timescale. However, the intricate mechanism underlying how the force contributes to plate motion remains largely obscure. In this study, we discuss this issue with hope of expanding the understanding of plate motion.

2. An Ocean-Generated Force Driving Mechanism for Plate Motion

The continents are fixed on the top of the lithosphere, and the lithospheric plates connect to each other, this relationship allows the ocean-generated force (*i.e.*, ocean water pressure force) to interact with other forces that act on the lithospheric plates. Subsequently, we list the plausible forces that act on a sample continental plate (**Figure 1**) and discuss the physical nature of these forces. These forces can be classified into two categories: the forces acting on the parts of the continent that connect to the oceans and those acting at both the bottom surface of the continental plate and the parts of the continental plate that connect to adjacent plates. The forces acting on the parts of the continent that connect to the ocean are treated as ocean-generated forces, denoted as F_R on the right and F_L on the left. The horizontal forces decomposed from these forces are denoted as F_R' on the right and F_L' on the left. A more detailed description of the horizontal

forces generated by ocean water pressure may refer to Yang [33]. The force acting on the bottom surface of the continental plate arises from a coupling between the plate and underlying viscous asthenosphere. This force is called the basal friction force and is denoted as f_{base}. According to Forsyth & Uyeda [22], if there is thermal convection in the asthenosphere, f_{base} would be a driving force [16] [17] [20] [21]. If, instead, the asthenosphere is passive relative to plate motion, f_{base} would be a resistive force. Clennett *et al.* [35] recently treated mantle flow as a resisting force opposite to plate motions when plate reconstruction models are assessed. Here, we assume f_{base} to be a resistive force. Given that the continental plate moves toward the right, the forces acting on the parts of the continental plate that connect to adjacent plates include the collisional force from the plate on the right side and the push force from the ridge on the left side, they are denoted as F_C and F_{ridge}, respectively.

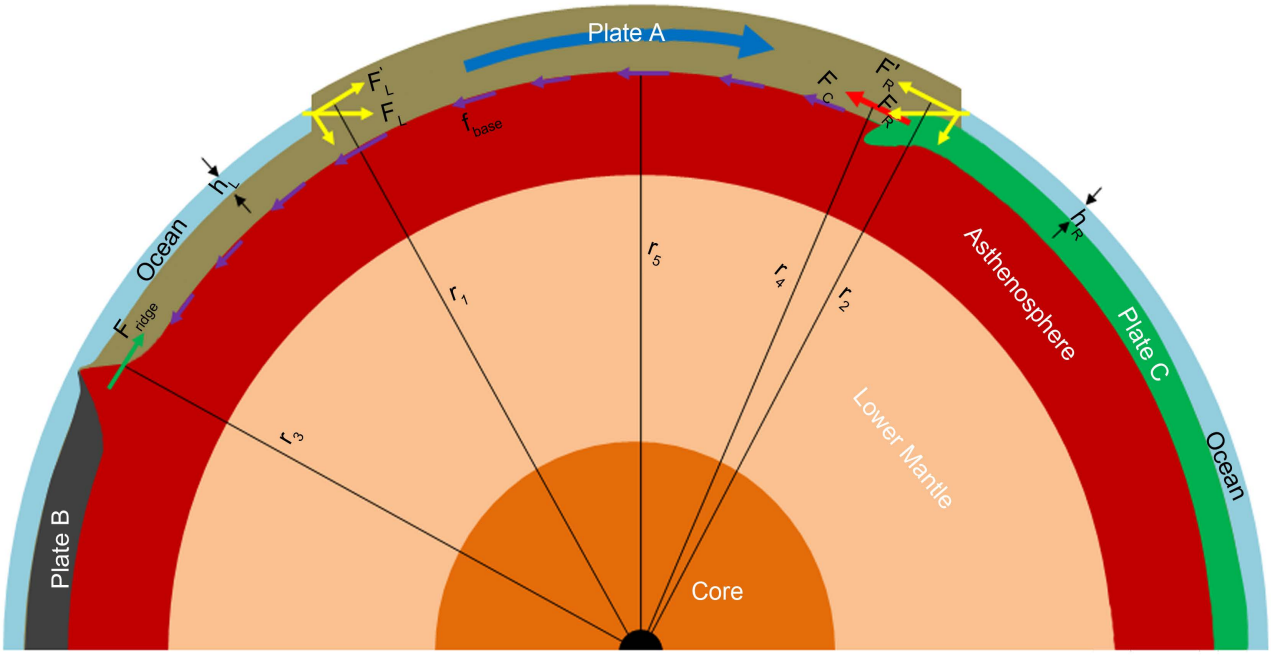

Figure 1. $F_L(F_R)$ represents the ocean-generated force on the left (right) side of Plate A, while $F_L'(F_R')$ and $F_L''(F_R'')$ denote the horizontal and vertical forces decomposed from the ocean-generated force, respectively. f_{base} denotes the basal friction force exerted by the underlying asthenosphere, while F_C and F_{ridge} denote the collisional force from Plate C on the right side and the push force from the ridge on the left side, respectively. h_L and h_R are the ocean depths on the left and right, respectively. r_1, r_2, r_3, r_4, and r_5 denote the distances of these forces to the Earth's center. Note that the ocean depth and lithospheric plate thickness are highly exaggerated.

Plate motion is conventionally understood as a rigid plate rotating about an axis that penetrates the Earth's center, and this rotation must be a consequence of the integrated effect of all torques acting on the plate [22] [26]. Following this understanding, we use torque balance to discuss the movement caused by these forces. According to **Figure 1**, a combined torque for Plate A may be written as

$$\tau = \left(r_1 F_L' - r_2 F_R'\right) + r_3 F_{\text{ridge}} - \left(r_4 F_C + r_5 f_{base}\right) \tag{1}$$

where the first term $\left(r_1F_L' - r_2F_R'\right)$ denotes the torque yielded by the final horizontal force, the second term r_3F_{ridge} denotes the torque yielded by the ridge push force, both of them represent the driving torque for the continental plate, and the third term ($r_4F_C + r_5f_{base}$) denotes the resisting torque, which hinders the movement of the continental plate. Taking into consideration the reality that the plate is too thin (e.g., less than few hundred kilometers) relative to the Earth's radius (e.g., more than six thousand kilometers), we approximate $r_1 = r_2 = r_3 = r_4 = r_5$.

Equation (1) provides three possibilities for the continental plate. If the driving torque is greater than the resisting torque, the combined torque is greater than zero, and the continental plate is subjected to an accelerating motion. Practically, it is impossible for the continental plate to undergo such an accelerating motion. If the driving torque is equal to the resisting torque, the combined torque is zero, and the continental plate would be subjected to a steady motion. If the driving torque is less than the resisting torque, the combined torque is less than zero, and the continental plate remains motionless.

Plate A's movement exhibited in **Figure 1** is parallel to that of Plate B and Plate C, this situation is rather idealized. Practically, the movements of most plates intersect with each other. For instance, the South American Plate moves northwest, the Nazca Plate moves eastward, the African Plate moves northeast, the Eurasian Plate moves eastward. These nonparallel movements would yield additional collisional forces and shearing forces between plates. If two plates are not moving in the opposite direction, the collisional and shearing forces between them may be driving; and if the two plates are moving in the opposite direction, the collisional and shearing forces between them may be resisting. Below, we develop two semi-analytic methods (I and II) to independently resolve plate motion.

2.1. Method I

It is assumed that the Earth's surface is covered with Plate A, Plate B, Plate C, Plate D, and others, and that Euler pole of each plate has been established (**Figure 2**). For Plate A (assumed to be continental), the horizontal force F_i (i = 1, 2, 3, 4, and 5) acts on the side of the continent that is fixed on top of Plate A. The horizontal force (F_1, for instance) yields a component (F_1', for instance) that is orthogonal to the rotation axis of the plate; this component then yields a torque (τ_1', for instance). The torques yielded by all the components decomposed from the horizontal forces are summed into first driving torque. The ridge push force $F_{r\text{-}i}$ (i = 1, 2, 3, and 4) acts on the edge of the plate, this force also yields a component that is orthogonal to the rotation axis; this component also yields a torque. The torques yielded by all the components decomposed from the ridge push forces are summed into second driving torque. Given that Plate A, Plate B, Plate C, and Plate D move eastward, southward, westward, and eastward, respectively, and that Plate D moves faster than Plate A, these make Plate A undergo a collisional driving force $F_{B\text{-}c}$ from Plate B, a shearing driving force $F_{D\text{-}s}$ from Plate D, a collisional resistive force $F_{C\text{-}c}$ from Plate C, a shearing resistive force $F_{B\text{-}s}$ from Plate B, and a

basal friction force F_{basal} from the underlying viscous asthenosphere. The collisional driving force $F_{B\text{-}c}$ and the shearing driving force $F_{D\text{-}s}$ also yield two components that are orthogonal to the rotation axis of the plate; these components also yield torques. The torques yielded by these two components are summed into third driving torque. The collisional resistive force $F_{C\text{-}c}$ and the shearing resistive force $F_{B\text{-}s}$ also yield two components that are orthogonal to the rotation axis; these components also yield torques. The torques yielded by these two components are summed into first resistive torque. The basal friction force F_{basal} yields second resistive torque.

Then, we divide these five sets of torques into two exerting parts: one, which includes the second driving torque and a little portion of the first and third driving torque, balances out the first resistive torque, and the other, which including the remaining portion of the first and third driving torque, balances the second resistive torque. Consequently, all these torque balances allow Plate A to be steadily rotated under the assumption that the acceleration and inertia of the plate are neglected. The remaining portion of the first and third driving torque is called the net driving torque, and the second resistive torque is called the net resistive torque. The balance between the net driving torque and the net resistive torque may be written as

$$\tau_{driving} - \tau_{basal} = 0 \tag{2}$$

where $\tau_{driving}$ is the net driving torque, $\tau_{driving} = \varepsilon\tau$, and ε is the ratio of the net driving torque to the first and third driving torque. As shown in **Figure 2(a)**, the component decomposed from a force (the horizontal force, for instance) may be written as $F_i = F_i\cos\eta_i$, and $\eta_i = \gamma_i - \lambda_i$, where γ_i is the inclination of this force to latitude. λ_i is the azimuth of arc P_iE with respect to latitude. This component yields a torque τ_i with respect to the rotation axis, *i.e.*, $\tau_i = r_iF_i$, where r_i denotes the lever arm distance of the component F_i, $r_i = R_{\text{earth}}\sin\varphi_{Pi}$, R_{earth} is the Earth's radius and R_{earth} = 6371 km, and φ_{Pi} is the angle of site P_i and the Euler pole. A sum of the torques yielded by the components, which are decomposed from the horizontal forces, collisional driving forces, and shearing driving forces, forms the first and third driving torque τ. τ_{basal} denotes the net resistive torque yielded by the basal friction force, it can be written as $\tau_{basal} = r_KF_{basal}$, where r_K denotes the lever arm distance of the basal friction force. According to the principle of fluid mechanics [36], the basal friction force may be expressed as $F_{basal} = \mu Au/y$, μ, A, u, and y are the viscosity of the asthenosphere, the plate's area, the plate's speed, and the thickness of the asthenosphere, respectively. Therefore, $u = y\tau_{driving}/\mu A$, this speed represents average level of the plate's movement. In general, the largest speed of a plate occurs at the plate's equator, while the smallest speed occurs at the location whose angle distance to the Euler pole is minimal or maximal. As shown in **Figure 2(b)**, we assume that the geometric center (*i.e.*, location K) of Plate A moves at the average speed, namely, $u = u_k$. And then, the speed of any location S within this plate may be expressed with $u_s = u_k\sin\varphi_s/\sin\varphi_k$, where $\varphi_s(\varphi_k)$ is the angle distance of location $S(K)$ to the Euler pole (*i.e.*, location E) relative to the Earth's

center. The speed u_s can be further decomposed into the longitudinal speed $u_{s\text{-}lo}$ and latitudinal speed $u_{s\text{-}la}$, and $u_{s\text{-}lo} = u_s\sin(\lambda_s - 90^\circ)$, $u_{s\text{-}la} = u_s\cos(\lambda_s - 90^\circ)$, where λ_s is the azimuth of arc SE with respect to latitude. The azimuth of the movement is then calculated through the longitudinal and latitudinal speeds. All these angles and distances (*i.e.*, η_b, γ_b, λ_b, λ_s, φ_{Pb}, φ_k, φ_s, r_b, r_K) may be further calculated through the latitudes and longitudes of related locations.

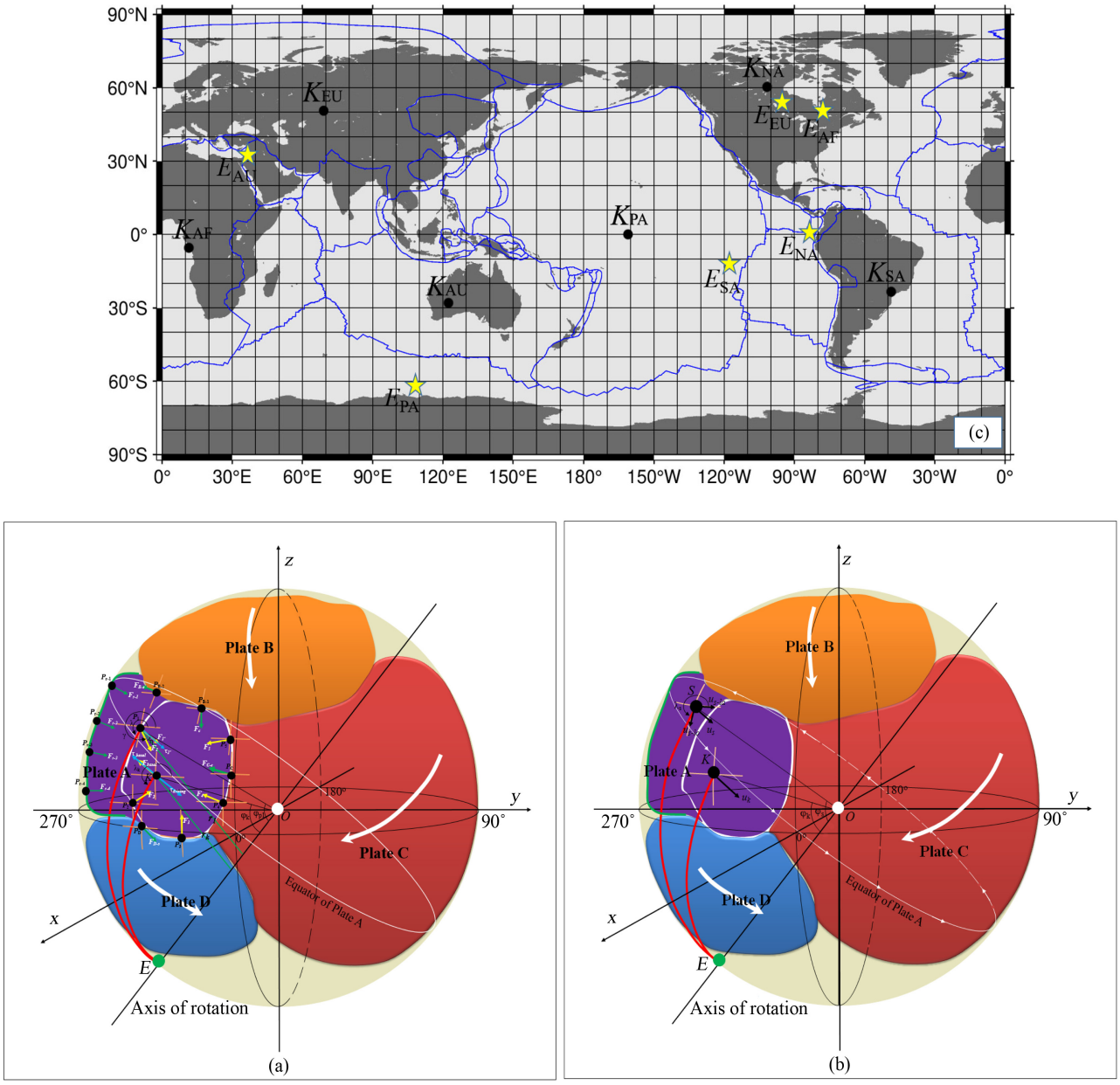

Figure 2. Modelling the torque balances for plate motion. (a) Geometry of ocean-generated horizontal forces, ridge push forces, collisional forces, and shearing forces over a spherical frame. The white oval within Plate A represents the scope of the continent. The green line denotes the oceanic ridge. The pink lines beneath the locations (black dots) denote the latitudinal and longitudinal directions. (b) Decomposing the average movement of the plate into the movement of any location. The location K and E are the geometric center of Plate A and its Euler pole, respectively. (c) Exhibiting the geometric centers (black dots) of the six selected plates and the established Euler pole locations (yellow stars) over a planar frame.

Here, we use six plates (South American, African, Eurasian, North American, Australian, and Pacific) to demonstrate their movements. In order to simplify the following deduction, we plot globally tectonic plates into a grid of 10˚ × 10˚ and use these grid nodes, which are within plate, to obtain the geometric center of each plate. The geometric center is approximately calculated through the average of the latitudes and longitudes of these nodes. The Euler pole location of each of these plates is cited from the GSRM v.2.1 [37]. Both the geometric center of each plate and its Euler pole location are exhibited in **Figure 2(c)**.

Besides these forces discussed above, the additional forces (*i.e.*, collisional and shearing) for these plates need to be considered. As exhibited in **Figure 3**, the African, Indian, and Australian plates provide the collisional driving forces $F_{\text{AF-EU-C}}$, $F_{\text{IN-EU-C}}$, and $F_{\text{AU-EU-C}}$ for the Eurasian Plate, respectively. The Nazca plate provides a collisional driving force $F_{\text{Naz-SA-C}}$ for the South American Plate. The Eurasian Plate provides a shearing resistive force $F_{\text{EU-NA-S}}$ for the North American Plate; vice versa, the North American Plate provides a shearing driving force $F_{\text{NA-EU-S}}$ for the Eurasian Plate. The Australian, North American, and Eurasian Plates provide the collisional driving forces $F_{\text{AU-PA-C}}$, $F_{\text{NA-PA-C}}$, and $F_{\text{EU-PA-C}}$ for the Pacific Plate, respectively. The Australian, North American, and Eurasian Plates provide the collisional driving forces $F_{\text{AU-PA-C}}$, $F_{\text{NA-PA-C}}$, and $F_{\text{EU-PA-C}}$ for the Pacific Plate, respectively. It's important to note that, while slab pull has widely been linked to the Pacific Plate, Doglioni and Panza [38] made a comprehensive review on this force and presented a long list of geometric, kinematic, and mechanical arguments against it as the primary driving force. This conclusion is recently strengthened by Faccincani *et al.* [39]. These authors found that the lithospheric mantle density

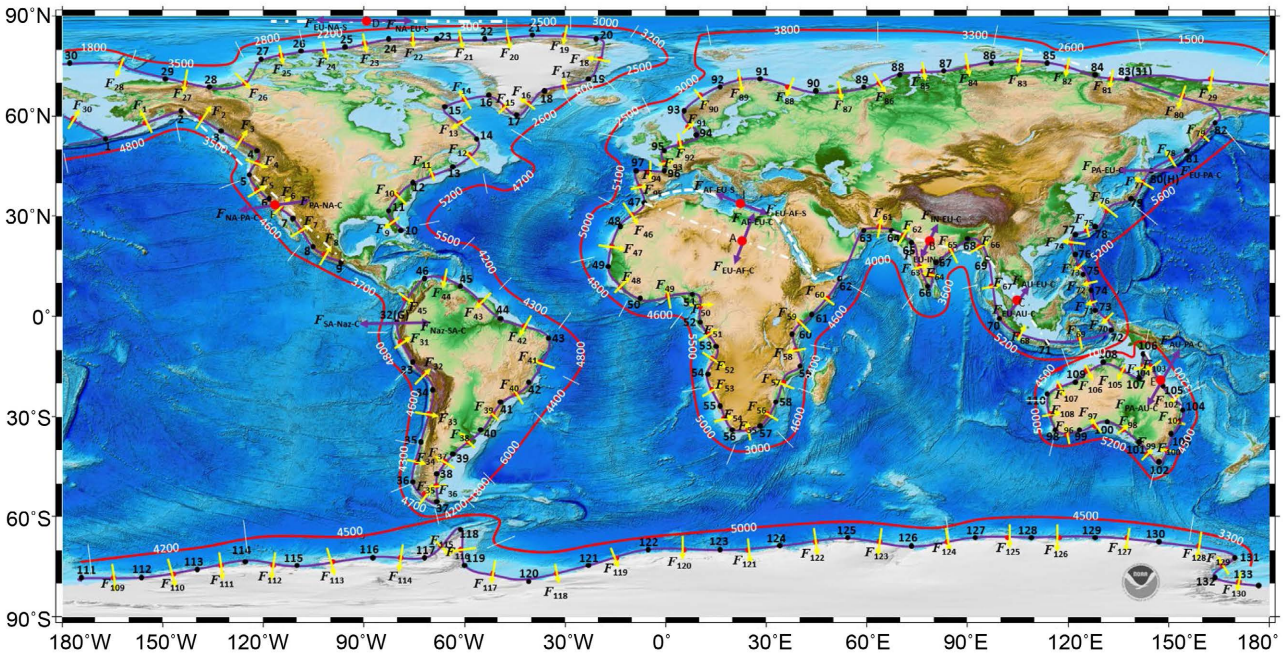

Figure 3. Ocean-generated horizontal forces (yellow arrows) and related collisional/shearing forces (purple arrows). The original map is from Yang (2024) [33].

structure can be affected by variations in thermal regimes and bulk composition, and their results suggest that the lithospheric mantle is not denser than the underlying asthenospheric mantle. A difference in density between the lithospheric mantle and the underlying asthenospheric mantle means that the oceanic plate, which consists of the lithospheric crust and mantle, is unlikely to sink, forming a "negative" buoyancy to drive plate motion. Taking into account this present status, we temporarily neglect slab pull in the modelling here but will discuss it latterly. The details of these collisional and shearing forces are listed in **Table 1**. It is worth noting that the magnitude and direction of these forces are artificially given, potentially causing discrepancies with reality. A precise determination of these forces requires an in-depth investigation of plate boundary structures, but is not feasible within the scope of this study due to individual effort constraints. The resultant torques from all related forces are listed in **Table 2**.

The asthenosphere viscosity is not yet exactly determined. Many numerical studies using glacial isostatic adjustment and geoid modelling have shown that asthenospheric viscosity ranges from 10^{17} to 10^{20} Pas [40]-[49]. Laboratory experiments, however, suggested that the magnitude of the asthenospheric viscosity could be substantially different from those constrained by numerical studies. The viscosity is variable and likely related to the thermodynamic state, grain size, composition of the medium, and state of stress [50]. Both the melt contents of the asthenosphere and the water in the asthenosphere may greatly affect the viscosity [51] [52]. Hirth and Kohlstedt [52] reported a variable viscosity profile for a melt-free oceanic lithosphere with a mean value of ~10^{18} Pas. These authors [53] [54] concluded that, in consideration of the water- and melt-rich layers characterized by much lower viscosities, a strong vertical variability of viscosity may be more realistic. The asthenosphere's effective viscosity can be greatly lowered to 10^{15} Pas if the water content in the case of both diffusion and dislocation creep is included

Table 1. Given collisional and shearing forces between plates.

Control site			F_i		Inclination to latitude, east (γ_i)
j	Longitude	Latitude	i	N ($\times 10^{17}$)	Degrees
A	26.50˚	22.40˚	AF-EU-C (EU-AF-C)	4.2	66.13˚ (246.13˚)
B	21.05˚	80.92˚	IN-EU-C (EU-IN-C)	1.3	71.47˚ (251.47˚)
C	12.15˚	104.09˚	AU-EU-C (EU-AU-C)	1.5	54.74˚ (234.74˚)
D	88.00˚	84.59˚	NA-EU-S (EU-NS-S)	4.0	0.00˚ (180.00˚)
E	−19.64˚	148.17˚	AU-PA-C (PA-AU-C)	1.0	55.00˚ (235.00˚)
F	41.22˚	238.99˚	NA-PA-C (PA-NA-C)	3.0	185.00˚ (5.00˚)
G	−2.20˚	278.96˚	Naz-SA-C (SA-Naz-C)	0.2	0.00˚ (180.00˚)
H	43.68˚	144.98˚	PA-EU-C (EU-PA-C)	0.1	180.00˚ (0.00˚)
I	20.68˚	35.70˚	AF-EU-S (EU-AF-S)	0.8	170.00˚ (350.00˚)

Notes: related sites refer to **Figure 3**.

Table 2. (a) Parameters for the torques of six selected plates in the method I. (b) Parameters for the torques of six selected plates in the method I (continued). (c) Parameters for the torques of six selected plates in the method I (continued). (d) Parameters for the torques of six selected plates in the method I (continued).

(a)

Plate	Eule pole		No.	Angle between horizontal force and its decomposed force	Decomposed force	Angle of site P_i and Eule pole	Earth's radius	Lever arm distance	Torque
	E		i	η_i	$F_{i'}$	φ_{pi}	R_{earth}	r_i	τ_i
	Latitude	Longitude		Degrees	N ($\times 10^{17}$)	Degrees	m ($\times 10^3$)	m ($\times 10^3$)	N m ($\times 10^{23}$)
North America	2.19˚	276.25˚	1	97.27˚	0.2497	79.30˚	6371.00	6260.27	−1.5632
			2	92.72˚	0.0574	72.92˚	6371.00	6089.89	−0.3493
			3	86.94˚	0.0381	63.32˚	6371.00	5692.78	0.2170
			4	316.47˚	0.4054	55.68˚	6371.00	5261.94	2.1332
			5	353.88˚	0.9497	49.51˚	6371.00	4845.13	4.6012
			6	358.11˚	1.3675	39.66˚	6371.00	4066.52	5.5611
			7	343.60˚	0.4981	30.91˚	6371.00	3272.51	1.6300
			8	14.05˚	0.7108	23.29˚	6371.00	2519.47	1.7909
			9	212.77˚	0.8725	26.03˚	6371.00	2795.38	−2.4389
			10	115.64˚	0.6455	33.23˚	6371.00	3490.93	−2.2536
			11	129.96˚	0.9586	41.83˚	6371.00	4249.32	−4.0733
			12	101.72˚	0.2780	50.75˚	6371.00	4933.75	−1.3715
			13	227.96˚	0.3704	58.02˚	6371.00	5404.09	−2.0014
			14	129.97˚	0.4880	63.81˚	6371.00	5717.10	−2.7900
			15	65.38˚	0.1302	65.61˚	6371.00	5802.46	0.7556
			16	90.08˚	0.0004	69.11˚	6371.00	5952.09	−0.0023
			17	109.75˚	0.0010	75.74˚	6371.00	6174.81	−0.0061
			18	207.62˚	0.6048	81.54˚	6371.00	6301.68	−3.8112
			19	281.86˚	0.0218	83.53˚	6371.00	6330.41	0.1377
			20	254.21˚	0.0165	81.97˚	6371.00	6308.49	−0.1042
			21	258.36˚	0.0002	81.06˚	6371.00	6293.59	−0.0013
			22	251.94˚	0.0175	80.59˚	6371.00	6285.20	−0.1102
			23	318.90˚	0.0601	79.05˚	6371.00	6255.08	0.3762
			24	282.85˚	0.0155	77.95˚	6371.00	6230.53	0.0969
			25	303.63˚	0.0668	77.54˚	6371.00	6220.87	0.4153
			26	295.24˚	0.2553	76.48˚	6371.00	6194.44	1.5815
			27	223.62˚	0.2277	79.34˚	6371.00	6261.13	−1.4256
			28	252.92˚	0.1328	85.13˚	6371.00	6347.96	−0.8430
			29	268.96˚	0.0032	93.29˚	6371.00	6360.48	−0.0203
			30	240.52˚	0.0001	93.27˚	6371.00	6360.61	−0.0009
			EU-NA-S	47.10˚	2.7231	89.81˚	6371.00	6370.96	−17.3490
			PA-NA-C	35.15˚	1.6353	51.43˚	6371.00	4981.26	8.1461
								total	−13.0728

Note: The negative symbol "-" beneath torque denotes counterclockwise with respect to the axis of rotation.

(b)

Plate	Eule pole		No.	Angle between horizontal force and its decomposed force	Decomposed force	Angle of site P_i and Eule pole	Earth's radius	Lever arm distance	Torque
	E		i	η_i	$F_{i'}$	φ_{pi}	R_{earth}	r_i	τ_i
	Latitude	Longitude		Degrees	N ($\times 10^{17}$)	Degrees	m ($\times 10^3$)	m ($\times 10^3$)	N m ($\times 10^{23}$)
South America	−14.10˚	242.14˚	31	94.63˚	0.1175	38.23˚	6371.00	3942.62	−0.4635
			32	117.64˚	0.5594	40.64˚	6371.00	4149.63	−2.3212
			33	75.71˚	0.4446	45.73˚	6371.00	4561.87	2.0280
			34	68.24˚	0.4722	42.53˚	6371.00	4306.96	2.0337
			35	107.25˚	0.2812	41.10˚	6371.00	4188.48	−1.1777
			36	247.03˚	0.0605	48.92˚	6371.00	4802.51	−0.2907
			37	214.43˚	0.0958	50.48˚	6371.00	4914.25	−0.4707
			38	188.74˚	1.7689	54.93˚	6371.00	5214.44	−9.2238
			39	200.24˚	1.9216	61.42˚	6371.00	5594.69	−10.7506
			40	181.06˚	1.4396	66.20˚	6371.00	5829.25	−8.3917
			41	212.82˚	1.3693	71.37˚	6371.00	6037.15	−8.2667
			42	301.17˚	0.8180	74.55˚	6371.00	6140.76	5.0232
			43	286.96˚	0.4041	66.24˚	6371.00	5831.18	2.3565
			44	253.52˚	0.0936	58.47˚	6371.00	5430.40	−0.5084
			45	347.68˚	1.6887	58.25˚	6371.00	5417.83	9.1491
			Naz-SA-C	71.58˚	0.0632	38.26˚	6371.00	3945.32	0.2493
								total	−21.0251
Africa	49.66˚	281.92˚	46	70.14˚	0.3779	53.21˚	6371.00	5102.38	1.9283
			47	102.95˚	0.4016	56.52˚	6371.00	5314.13	−2.1344
			48	164.92˚	1.6163	66.57˚	6371.00	5845.72	−9.4486
			49	218.52˚	1.3702	77.78˚	6371.00	6226.76	−8.5319
			50	145.39˚	0.7668	86.18˚	6371.00	6356.85	−4.8747
			51	154.94˚	1.4114	94.61˚	6371.00	6350.43	−8.9632
			52	117.56˚	0.6083	101.46˚	6371.00	6243.91	−3.7983
			53	155.92˚	1.2945	108.55˚	6371.00	6039.87	−7.8188
			54	165.93˚	0.9259	116.64˚	6371.00	5694.53	−5.2727
			55	137.16˚	0.2165	121.92˚	6371.00	5407.37	−1.1709
			56	283.40˚	0.2429	123.18˚	6371.00	5331.97	1.2950
			57	275.06˚	0.0979	121.18˚	6371.00	5450.79	0.5337
			58	313.40˚	0.4141	115.74˚	6371.00	5738.80	2.3762
			59	264.22˚	0.0918	110.48˚	6371.00	5968.21	−0.5481
			60	259.19˚	0.2878	107.05˚	6371.00	6090.91	−1.7529
			EU-AF-C	7.26˚	4.1663	76.43˚	6371.00	6193.10	25.8022
			EU-AF-S	81.71˚	0.1154	88.57˚	6371.00	6369.01	−0.7349
									−23.1140

Note: the negative symbol "−" beneath torque denotes counterclockwise with respect to the axis of rotation.

(c)

late	Eule pole		No.	Angle between horizontal force and its decomposed force	Decomposed force	Angle of site P_i and Eule pole	Earth's radius	Length of lever arm	Torque
	E		i	η_i	$F_{i'}$	φ_{pi}	R_{earth}	r_i	τ_i
	Latitude	Longitude		Degrees	N ($\times 10^{17}$)	Degrees	m ($\times 10^3$)	m ($\times 10^3$)	N m ($\times 10^{23}$)
			67	258.40˚	0.4439	115.16˚	6371.00	5766.75	−2.5600
			68	149.71˚	2.0668	125.41˚	6371.00	5192.58	−10.7320
			69	334.71˚	0.0010	122.62˚	6371.00	5365.89	0.0051
			70	83.52˚	0.1608	114.29˚	6371.00	5806.87	0.9336
			71	79.27˚	0.1196	109.58˚	6371.00	6002.67	0.7181
			72	37.66˚	0.4566	106.33˚	6371.00	6114.00	2.7916
			73	49.55˚	0.8144	102.01˚	6371.00	6231.63	5.0750
			74	21.11˚	0.6848	96.81˚	6371.00	6326.02	4.3322
			75	81.02˚	0.1270	92.43˚	6371.00	6365.29	0.8082
			76	62.48˚	0.8568	84.59˚	6371.00	6342.61	5.4341
			77	40.27˚	1.3288	73.63˚	6371.00	6112.77	8.1227
			78	57.60˚	0.7856	64.43˚	6371.00	5747.16	4.5148
			79	31.07˚	1.5750	54.93˚	6371.00	5214.08	8.2124
			80	171.95˚	0.7962	49.33˚	6371.00	4832.06	−3.8475
			81	154.76˚	0.1390	49.63˚	6371.00	4854.19	−0.6747
			82	133.27˚	0.1370	48.52˚	6371.00	4772.97	−0.6539
			83	174.32˚	0.1546	48.39˚	6371.00	4763.58	−0.7366
Eurasia	55.38˚	264.59˚	84	23.23˚	0.2161	49.86˚	6371.00	4870.34	−1.0527
			85	11.67˚	0.2564	51.62˚	6371.00	4994.15	−1.2803
			86	34.19˚	0.3098	53.25˚	6371.00	5104.74	−1.5816
			87	11.01˚	0.4192	54.21˚	6371.00	5167.62	−2.1662
			88	175.74˚	0.3857	52.24˚	6371.00	5036.62	1.9426
			89	0.46˚	0.5334	48.88˚	6371.00	4799.38	−2.5601
			90	45.07˚	0.0023	47.33˚	6371.00	4684.66	−0.0107
			91	5.85˚	1.1744	50.70˚	6371.00	4930.18	−5.7901
			92	44.78˚	0.2217	45.84˚	6371.00	4570.16	1.0132
			93	102.94˚	0.1687	55.45˚	6371.00	5247.62	−0.8854
			94	81.57˚	0.1424	54.98˚	6371.00	5217.66	0.7429
			95	122.84˚	0.7633	57.09˚	6371.00	5348.90	−4.0826
			AF-EU-C	174.37˚	4.1797	82.54˚	6371.00	6317.01	−26.4034
			IN-EU-C	178.65˚	1.2996	103.51˚	6371.00	6194.68	−8.0509
			AU-EU-C	166.77˚	1.4602	110.51˚	6371.00	5967.18	−8.7133
			NA-EU-S	106.31˚	1.1233	36.62˚	6371.00	3800.34	−4.2691
			PA-EU-C	97.84˚	0.0136	68.57˚	6371.00	5930.61	0.0808
			AF-EU-S	29.84˚	0.6940	93.37˚	6371.00	6359.96	4.4136
								total	−36.9103

Note: the negative symbol "−" beneath torque denotes counterclockwise with respect to the axis of rotation.

(d)

Plate	Eule pole		No.	Angle between horizontal force and its decomposed force	Decomposed force	Angle of site P_i and Eule pole	Earth's radius	Length of lever arm	Torque
	E		i	η_i	$F_{i'}$	φ_{pi}	R_{earth}	r_i	τ_i
	Latitude	Longitude		Degrees	N ($\times 10^{17}$)	Degrees	m ($\times 10^3$)	m ($\times 10^3$)	N m ($\times 10^{23}$)
Australia	33.31˚	36.38˚	96	254.20˚	0.3723	110.26˚	6371.00	5976.79	−2.22515
			97	241.45˚	0.4908	107.86˚	6371.00	6063.97	−2.97597
			98	182.17˚	1.4429	115.09˚	6371.00	5769.94	−8.32561
			99	170.88˚	1.1458	123.09˚	6371.00	5337.79	−6.11606
			100	294.07˚	0.3880	126.38˚	6371.00	5129.41	1.990312
			101	283.24˚	0.1994	126.78˚	6371.00	5102.73	1.01746
			102	334.60˚	0.4275	123.59˚	6371.00	5307.41	2.268856
			103	331.54˚	0.5998	114.69˚	6371.00	5788.35	3.471845
			104	106.97˚	0.0001	110.38˚	6371.00	5972.19	−0.0007
			105	261.10˚	0.0001	106.09˚	6371.00	6121.32	−0.0006
			106	66.81˚	0.0002	98.56˚	6371.00	6300.01	0.0013
			107	64.56˚	0.3686	94.58˚	6371.00	6350.68	2.340567
			108	178.47˚	3.0974	104.19˚	6371.00	6176.62	−19.1313
			EU-AU-C	15.71˚	1.4440	64.82˚	6371.00	5765.39	8.325007
			PA-AU-C	3.92˚	0.9977	118.47˚	6371.00	5600.47	5.587377
								total	−13.7727
Pacific	−63.09˚	109.63˚	AU-PA-C	87.49˚	0.0437	50.72˚	6371.00	4931.80	0.2157
			NA-PA-C	39.99˚	2.2984	143.46˚	6371.00	3793.07	−8.7181
			EU-PA-C	12.55˚	0.0976	110.42˚	6371.00	5970.70	0.5828
								total	−7.9195

Note: the negative symbol "−" beneath torque denotes counterclockwise with respect to the axis of rotation.

[55]. Scoppola *et al.* [54] conducted a more detailed review of asthenospheric viscosity and concluded that the presently accepted values of viscosity might be reduced through a combined experiment including these parameters (*i.e.*, melt content, water content, mechanical anisotropy, and shear localization). A "superweak", low-viscosity asthenosphere supported by recent observations is being accepted by the geophysical community [47] [49] [56]-[61]. Jordan [62] treated the asthenospheric thickness as 300 km. Taking into account the present status of the viscosity and thickness of the asthenosphere above, we adopt $y = 300$ km for each of the six selected plates, $\mu = 10^{18}$ Pas for the South American, African, North American, and Eurasian plates, $\mu = 0.6 \times 10^{18}$ Pas for the Australian Plate, and $\mu = 0.12 \times 10^{18}$ Pas for the Pacific Plate. The other parameters (*i.e.*, plate area, the ratio of the net driving torque and the first and third driving torque) and the resultant

average movements of these plates are listed in Table 3.

There have been many plate motion models (*i.e.*, GSRM, NUVEL-1, and MORVEL) that include global navigation satellite systems (GNSS) and paleomagnetic data. For instance, GSRM v.2.1 includes more than 6739 continuous GPS velocity measurements [37]. The movements reproduced by these models may approximately represent observations. Here, the movements of 450 locations (41 for the South American Plate, 70 for the African Plate, 93 for the North American Plate, 95 for the Eurasian Plate, 47 for the Australian Plate, and 104 for the Pacific Plate) are reproduced by GSRM v.2.1. The modelled and reproduced movements are then compared in Figure 4. The Root Mean Square Error (RMSE) of the modelled speed against the reproduced speed for a plate is expressed as

$$\mathrm{RMSE} = \sqrt{\sum_0^m \left(u_m(i) - u_o(i)\right)^2 / m} \tag{3}$$

where $u_m(i)$ represents the speed of a location (i) calculated by our model, $u_o(i)$ represents the speed reproduced by GSRM v.2.1, and m is the total number of locations in the plate. It can been found that the modelled movements for these locations are well consistent with the reproduced movements in both speed and azimuth, the RMSE of the modelled speed against the reproduced speed for the South American, African, North American, Eurasian, Australian, and Pacific plates is 0.91, 3.76, 2.77, 2.31, 7.43, and 1.95 mm/yr, respectively.

2.2. Method II

We assume that the Earth's surface is covered with Plate A, Plate B, Plate C, Plate D, and others (Figure 5). For Plate A (assumed it to be continental), it undergoes the ocean-generated horizontal force F_i (i = 1, 2, 3, 4, and 5), the ridge push force $F_{r\text{-}i}$ (i = 1, 2, 3, and 4), the collisional driving force $F_{B\text{-}c}$, the shearing driving force $F_{D\text{-}s}$, the collisional resistive force $F_{C\text{-}c}$, the shearing resistive force $F_{B\text{-}s}$, and the basal friction force F_{basal}. One horizontal force (F_1, for instance) yields a torque (τ_1,

Table 3. The net driving torques and their resultant movements for these selected plates in the method I.

Plate	Area	Ratio	Net driving torque	Geometric center of the plate			Lever arm distance for basal friction force	Movement
	A	ε	$\tau_{driving}$	K		φ_k	r_k	u
	km^2		N m (10^{23})	Latitude	Longitude	Degrees	m (10^3)	mm/yr
South America	43,600,000	0.15	3.18	−24.39˚	313.66˚	67.63˚	5891.49	11.73
Africa	61,300,000	0.64	14.74	−5.57˚	13.43˚	95.22˚	6344.59	35.85
North America	75,900,000	0.79	10.39	59.57˚	256.88˚	59.31˚	5478.57	23.64
Eurasia	67,800,000	0.31	11.51	50.32˚	68.84˚	73.49˚	6108.39	26.29
Australia	47,000,000	0.91	12.55	−28.30˚	122.98˚	102.51˚	6219.65	67.72
Pacific	103,300,000	0.75	5.98	0.10˚	198.65˚	89.64˚	6370.88	71.61

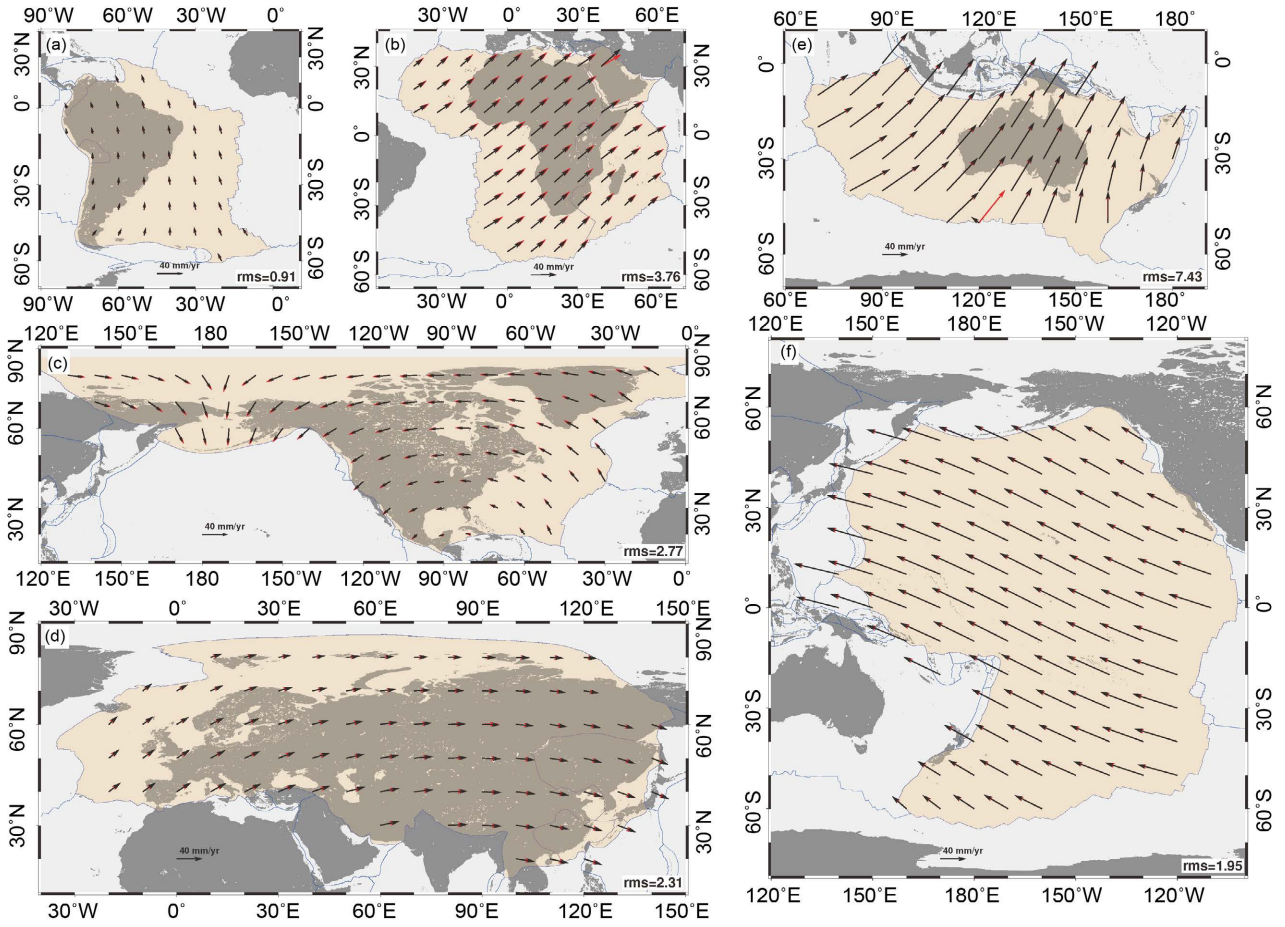

Figure 4. The reproduced movements from GSRM v.2.1 (black arrows) verse the calculated movements from our model (red arrows) in the method I. (a)-(f) are the South American, African, North American, Eurasian, Australian, and Pacific plates, respectively.

for instance), another horizontal force (F_2, for instance) yields another torque (τ_2, for instance), a combination of these two torques results in a new torque ($\tau_{1\text{-}2}$, for instance), this new torque then combines the torque yielded by third horizontal force to form another new torque. Subsequently, the torques yielded by all the horizontal forces are combined into a final torque. The collisional driving force $F_{B\text{-}c}$ yields a torque, the shearing driving force $F_{D\text{-}s}$ yields a torque, the final torque combines these two torques to firm first driving torque. The collisional resistive force $F_{C\text{-}c}$ and the shearing resistive force $F_{B\text{-}s}$ also yield two torques, they combine to firm first resistive torque. The basal friction force F_{basal} yields second resistive torque. The ridge push force $F_{r\text{-}i}$ (i = 1, 2, 3, and 4) also yields a torque, the torques yielded by all the ridge push forces are combined into second driving torque.

Then, we divide these four sets of torques into two exerting parts: one, which includes the second driving torque and a portion of the first driving torque, balances out first the resistive torque, and the other, which including the remaining portion of the first driving torque, balances the second resistive torque. Consequently, all these torque balances allow Plate A to be steadily rotated under the assumption that the acceleration and inertia of the plate are neglected. The

remaining portion of the first driving torque is called the net driving torque, and second resistive torque is called the net resistive torque. We assume that the net driving torque exerts on the geometric center (*i.e.*, location *K*) of Plate A, this makes the plate move along a big circle that represents the equator of this Plate. And then, the balance between the net driving torque and the net resistive torque may be expressed with Equation (2). According to **Figure 5(a)**, a force F_i yields a torque τ_i with respect to the Earth's center, *i.e.*, $\tau_i = R_{\text{earth}}F_i$, where R_{earth} is the Earth's radius and R_{earth} = 6371 km. The combination of two torques follows the trigonometric principle and may be written as

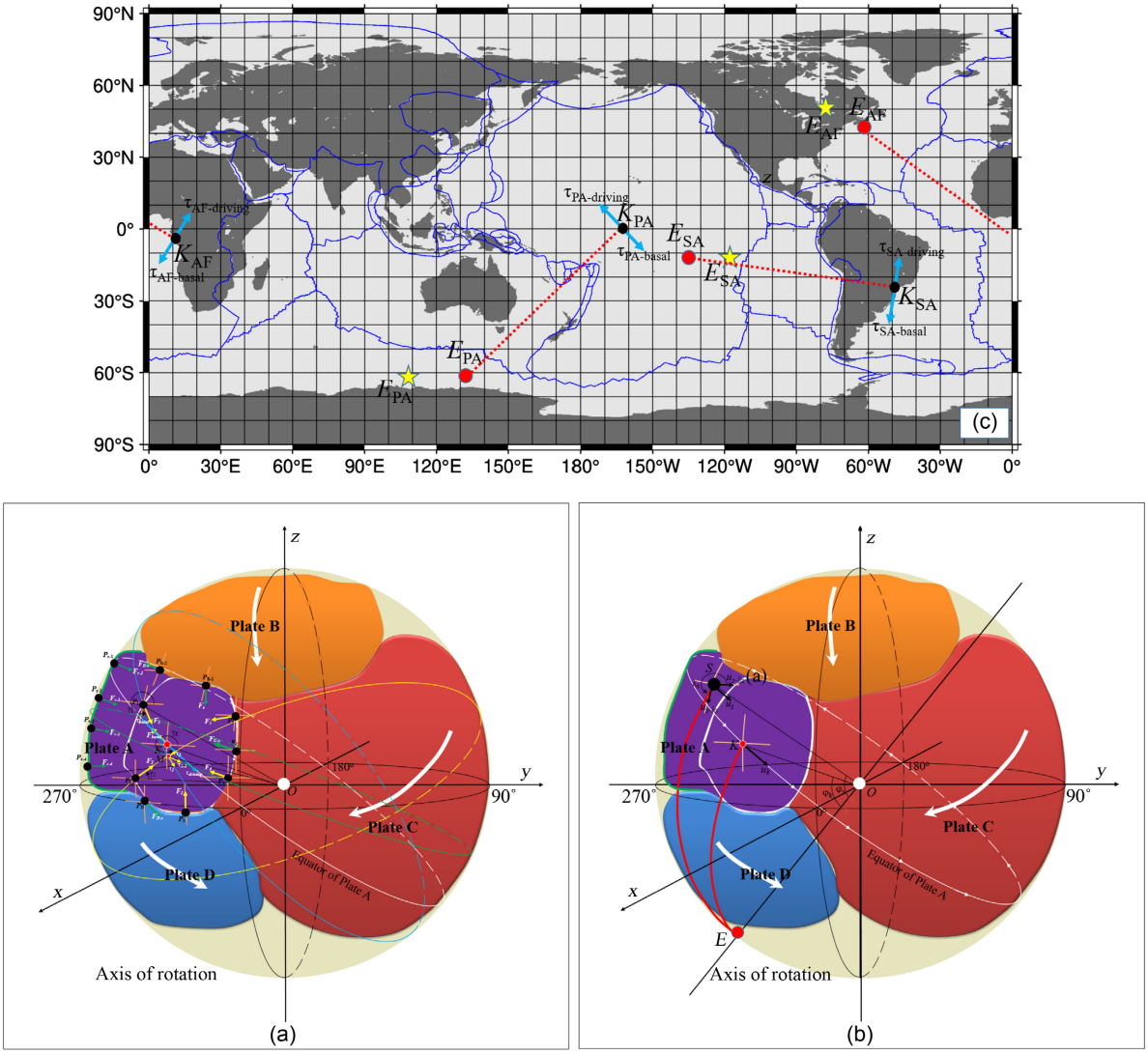

Figure 5. Modelling the torque balances for plate motion. (a) Geometry of ocean-generated horizontal forces, ridge push forces, collisional forces, and shearing forces over a spherical frame. The large light blue and yellow circles denote the orientations of the torques yielded by the horizontal force F_1 and F_2, the large green circle denotes the orientation of the combined torque of these two torques, and the large white circle denotes the possible orientation of the first driving torque. (b) Decomposing the average movement of the plate into the movement of any location. The location *K* and *E* are the geometric center of the plate and its Euler pole, respectively. (c) Exhibiting the torque balance of the selected plates over a planar frame. The calculated Euler pole locations (red dots) are compared to the established Euler pole locations (yellow stars).

$$\tau_j^2 = \tau_i^2 + \tau_{i+1}^2 + 2\tau_i\tau_{i+1}\cos\left(\gamma_i - \gamma_{i+1}\right) \quad (4)$$

where τ_j is the combined torque, τ_i and τ_{i+1} are the torque yielded by the force F_i and F_{i+1}, respectively. γ_i and γ_{i+1} denote the inclination of the forces F_i and F_{i+1} to latitude, respectively. τ_{basal} denotes the net resistive torque yielded by the basal friction force, it can be written as $\tau_{basal} = R_{\text{earth}}F_{basal}$. According to the principle of viscous fluid mechanics, the basal friction force may be expressed as $F_{basal} = \mu Au/y$, μ, A, u, and y are the viscosity of the asthenosphere, the plate's area, the plate's speed, and the thickness of the asthenosphere, respectively. Therefore, $u = y\tau_{driving}/\mu A$, this speed represents average level of the plate's movement.

On the whole, the largest speed of a plate occurs at the plate's equator, while the smallest speed occurs at the location whose angle distance to the Euler pole is minimal or maximal. According to Figure 5(b), we assume that the geometric center (*i.e.*, location K) of Plate A moves at a speed of $u_k = \zeta u$, where ζ is an amplification coefficient of the average speed. And then, the speed of any location S within this plate may be expressed with $u_s = u_k\sin\varphi_s/\sin\varphi_k$, where $\varphi_s(\varphi_k)$ is the angle distance of location $S(K)$ to the Euler pole (*i.e.*, location E) relative to the Earth's center. The Euler pole is calculated through the location K and the orientation of the first driving torque τ. The speed u_s can be further decomposed into the longitudinal speed $u_{s\text{-}lo}$ and latitudinal speed $u_{s\text{-}la}$, and $u_{s\text{-}lo} = u_s\sin(\lambda_s\text{-}90^\circ)$, $u_{s\text{-}la} = u_s\cos(\lambda_s\text{-}90^\circ)$, where λ_s is the azimuth of arc SE with respect to latitude. The azimuth of the movement is then calculated through the longitudinal and latitudinal speeds. All these angles and distances (*i.e.*, γ_i, λ_s, φ_k, φ_s) may be calculated through the latitudes and longitudes of related locations.

We here use three plates (South American, African, and Pacific) to demonstrate the resultant movements. The geometric centers of these plates, the calculated Euler pole location, and the established Euler pole location cited from GSRM v.2.1 [37] are exhibited in Figure 5(c). A few other possible forces (*i.e.*, collisional and shearing) are considered for these plates. For example, the Eurasian Plate provides a collisional driving force $F_{\text{EU-AF-C}}$ and a shearing driving force $F_{\text{EU-AF-S}}$ for the African Plate. The Nazca plate provides a collisional driving force $F_{\text{Naz-SA-C}}$ for the South American Plate. The Australian, North American, and Eurasian plates provide the collisional driving force $F_{\text{AU-PA-C}}$, $F_{\text{NA-PA-C}}$, and $F_{\text{EU-PA-C}}$ for the Pacific Plate, respectively. Again, we temporarily neglect slab pull in the modelling here but will include it in the discussion of this study.

The details of these collisional and shearing forces have been exhibited in Figure 3 and listed in Table 1. The resultant torques from all related forces are listed in Table 4. The viscosity and thickness of the asthenosphere for these three plates are the same as that described in the method I. The other parameters (*i.e.*, plate area, the ratio of the net driving torque to the first driving torque, and the amplification coefficient) and the resultant average movements are listed in Table 5. The movements of 215 locations (41 for the South American Plate, 70 for the African Plate, and 104 for the Pacific Plate) are reproduced by GSRM v.2.1. The calculated and reproduced movements are compared in Figure 6. The Root Mean

Square Error (RMSE) of the calculated speed against the reproduced speed for these three plates is calculated through Equation (3). We find that the calculated movements for these locations are basically consistent with the reproduced movements in both speed and azimuth, the RMSE of the calculated speed against the reproduced speed for the South American, African, and Pacific plates is 0.98, 3.18, and 6.51 mm/yr, respectively. This result is not entirely as good as that demonstrated in the method I. One major cause for this is because the geometric center of a plate is strictly not calculated through the average of the latitudes and longitudes of those nodes. The less accurate first driving torque adds to the less accurate geometric center, naturally, the calculated Euler pole location and the resultant movement of the plate cannot be accurate. Even so, our goal has realized that a combination of the ocean-generated, ridge push, collisional force, and shearing forces may account for plate motion.

Table 4. (a) Parameters for the torques of three selected continental plates in the method II. (b) Parameters for the torques of three selected plates in the method II (continued).

(a)

Plate	Eule pole		No.	Horizontal force	Earth's radius	Torque	No.	Combined torque	
	E		i	F_i	R_{earth}	τ_i	j	τ_j	Inclination to latitude, east (γ_j)
	Latitude	Longitude		N ($\times 10^{17}$)	m ($\times 10^{3}$)	N m ($\times 10^{23}$)		N m ($\times 10^{23}$)	Degrees
South America	−14.68˚	224.18˚	31	1.4573	6371.00	9.2848	31	9.2815	22.92˚
			32	1.2059	6371.00	7.6829	31 - 32	16.8927	27.75˚
			33	1.8014	6371.00	11.4769	31 - 33	26.8242	12.22˚
			34	1.2737	6371.00	8.1145	31 - 34	34.5354	7.29˚
			35	0.9484	6371.00	6.0420	31 - 35	39.7562	12.02˚
			36	0.1551	6371.00	0.9883	31 - 36	39.7462	13.45˚
			37	0.1161	6371.00	0.7397	31 - 37	39.1661	14.12˚
			38	1.7897	6371.00	11.4020	31 - 38	34.9655	30.59˚
			39	2.0480	6371.00	13.0480	31 - 39	31.7450	52.47˚
			40	1.4398	6371.00	9.1732	31 - 40	35.3756	66.91˚
			41	1.6295	6371.00	10.3814	31 - 41	36.7958	83.30˚
			42	1.5804	6371.00	10.0688	31 - 42	27.5043	90.28˚
			43	1.3853	6371.00	8.8257	31 - 43	21.2133	105.00˚
			44	0.3300	6371.00	2.1025	31 - 44	21.1033	110.69˚
			45	1.7285	6371.00	11.0123	31 - 45	10.0916	109.90˚
			NA-SA-C	0.2000	6371.00	4.4597	31-NA-SA-C	9.5515	83.84˚

(b)

Plate	Eule pole		No.	Horizontal force	Earth's radius	Torque	No.	Combined torque	
	E		i	F_i	R_{earth}	τ_i	j	τ_j	Inclination to latitude, east (γ_j)
	Latitude	Longitude		N ($\times 10^{17}$)	m ($\times 10^3$)	N m ($\times 10^{23}$)		N m ($\times 10^{23}$)	Degrees
Africa	44.43˚	298.60˚	46	1.1123	6371.00	7.0867	46	7.0867	320.52˚
			47	1.7917	6371.00	11.4148	46 - 47	18.1425	334.91˚
			48	1.6739	6371.00	10.6648	46 - 48	24.8049	357.55˚
			49	1.7514	6371.00	11.1579	46 - 49	26.1494	22.67˚
			50	0.9317	6371.00	5.9357	46 - 50	32.0830	22.36˚
			51	1.5581	6371.00	9.9269	46 - 51	41.9838	23.48˚
			52	1.3150	6371.00	8.3777	46 - 52	48.8835	17.47˚
			53	1.4180	6371.00	9.0339	46 - 53	57.9100	17.86˚
			54	0.9546	6371.00	6.0816	46 - 54	63.9220	18.73˚
			55	0.2953	6371.00	1.8813	46 - 55	64.7399	20.24˚
			56	1.0480	6371.00	6.6768	46 - 56	60.9224	25.24˚
			57	1.1109	6371.00	7.0773	46 - 57	57.7443	31.35˚
			58	0.6026	6371.00	3.8393	46 - 58	54.2170	32.90˚
			59	0.9126	6371.00	5.8140	46 - 59	52.4030	38.84˚
			60	1.5344	6371.00	9.7756	46 - 60	50.6747	49.55˚
			EU-AF-C	4.2000	6371.00	26.7582	46-EU-AF-C	26.1669	66.52˚
			EU-AF-S	0.8000	6371.00	5.0968	46-EU-AF-S	27.8008	56.25˚
			NA-PA-C	3.0000	6371.00	19.1130	NA-PA-C	19.1130	185.00˚
Pacific	−65.25˚	136.77˚	*AU-PA-C	2.2000	6371.00	14.0162	NA-PA-C-AU-PA-C	14.7433	138.26˚
			EU-PA-C	0.1000	6371.00	0.6371	NA-PA-C-EU-PA-C	14.2742	136.56˚

Note: *denotes this force is changed from 1.0×10^{17} N listed in Table 1 to 2.2×10^{17} N.

Table 5. The net driving torques and their resultant movements for three selected plates in the method II.

Plate	Area	Ratio	Net driving torque	Geometric center of the plate			Earth's radius	Amplification coefficient	Movement
	A	ε	$\tau_{driving}$	K		φ_k	R_{earth}	ζ	u
	Km^2		N m (10^{23})	Latitude	Longitude	Degrees	m (10^3)		mm/yr
South America	43,600,000	0.30	2.8640	−24.39˚	313.66˚	83.84˚	6371.00	1.20	11.71
Africa	61,300,000	0.40	11.1202	−5.57˚	13.43˚	56.25˚	6371.00	1.20	32.33
Pacific	103,300,000	0.35	4.9960	0.10˚	198.65˚	136.56˚	6371.00	1.20	71.82

3. Discussion

3.1. Why May Ocean-Generated Force Contribute to Plate Motion?

Based on the principle of fluid mechanics [36], a plate moving over a fluid may be expressed with a force balance equation $F = \mu A u / y$, where F, μ, A, u, and y

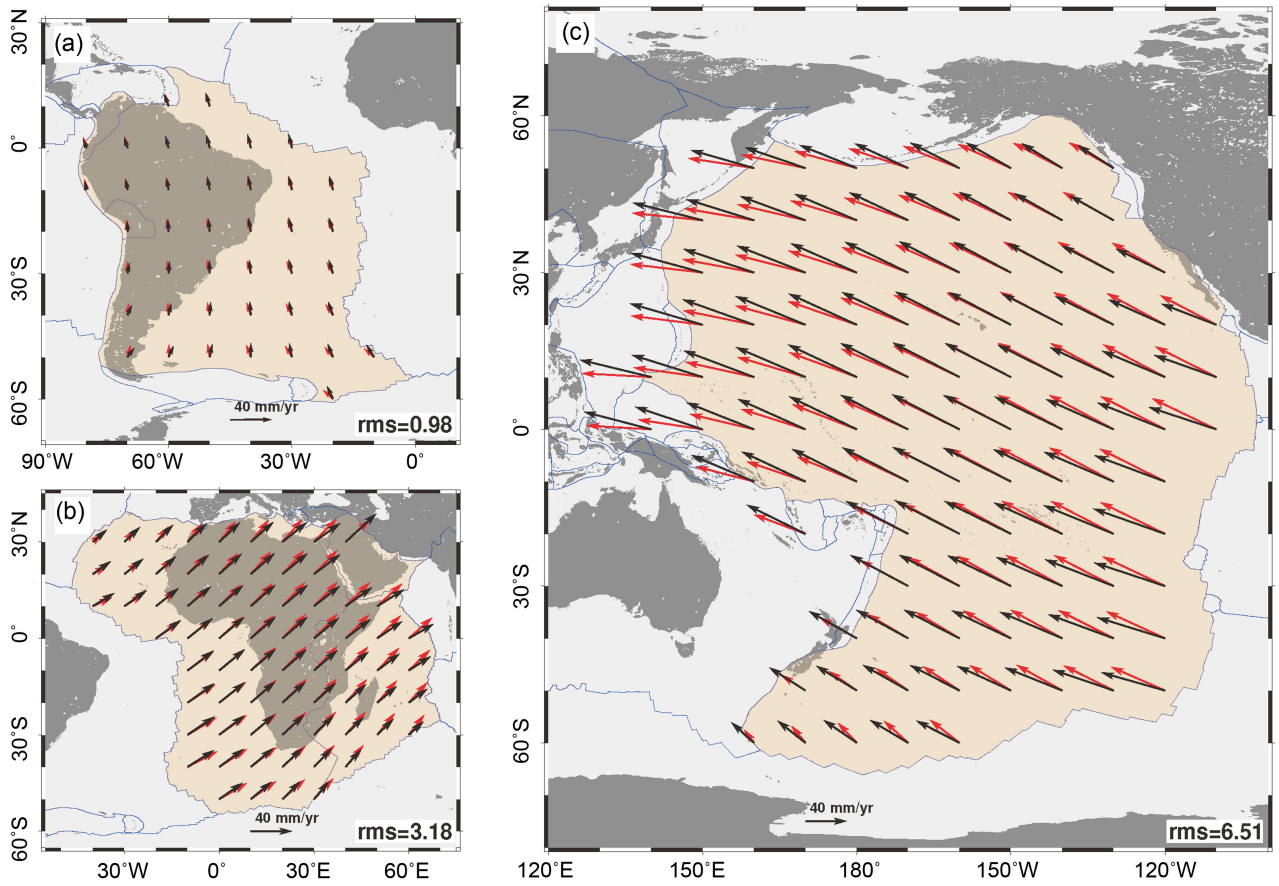

Figure 6. The reproduced movements from GSRM v.2.1 (black arrows) verse the calculated movements from our model (red arrows) in the method II. (a), (b), and (c) are the South American, African, and Pacific plates, respectively.

represent the driving force, the fluid's viscosity, the plate's area, the plate's speed, and the thickness of the fluid, respectively. This relationship is illustrated in **Figure 7(a)**. Practically, the lithospheric plates consist of the crust and the upper mantle and extend about 100 km below Earth's surface, most of them have a horizontal dimension of several thousands of kilometers. Beneath the plates is the more fluid asthenosphere, which extends from roughly 100 km to 700 km below Earth's surface. These features allow us to apply the equation above to estimate the force that is necessary to maintain the movement of the lithosphere over the asthenosphere, where F, μ, A, u, and y now denote the driving force, the asthenosphere's viscosity, the lithosphere's area, the lithosphere's speed, and the asthenosphere's thickness, respectively (**Figure 7(b)**). The lithosphere's area and the asthenosphere's thickness have been well established, while the viscosity of the asthenosphere remains a high uncertainty, which has been extensively discussed in Section 5. We here assume the lithosphere to move at a speed u = 3 cm/yr, although the fact is not so because it has been fractured into individual plates whose movements are various in both speed and direction. Given y = 300 km (Jordan, 1974), A = 510,000,000 km^2 [32], and $\mu = 10^{15}$ - 10^{20} Pas, the driving force calculated through the equation above ranges from 1.6172×10^{15} to 1.6172×10^{20} N.

This result indicates that, if we want the lithosphere to move at a speed of 3.0 cm per year over the asthenosphere, a driving force of 10^{15} - 10^{20} N is necessary, and that this force is simultaneously countered by a resistive force from the asthenosphere, creating a force balance that enables the movement to be realized steadily. And now, we ideally divide the lithosphere into individual plates, and exert a driving force to one of these plates, the plate encounters resistance from adjacent plates and the underlying viscous asthenosphere. Since all of plates are physically attached to the underlying asthenosphere, the upper limit of the total resistance force undergone by this plate would be 10^{15} - 10^{20} N. Thus, for a lithospheric plate to move over the underlying asthenosphere, a driving force whose magnitude matches this upper limit of the total resistance force is required.

The continents are fixed on the top of the lithosphere that is composed of individual plates, and the plates connect to each other, this frame enables the ocean-generated force to be laterally transferred to the plates. As shown by Yang [33], the ocean-generated force (*i.e.*, the horizontal force F_i) is generally at a magnitude of 10^{17} N, this amount has fallen within the range of the upper limit of the total resistance force. As illustrated in **Figure 7(c)**, three plates are totally designed in the model; along the vertical direction, the weight of each plate is balanced out by the support from the asthenosphere; thus, we only need to discuss the force balance along the horizontal direction. F_{AR}, F_{AL}, F_{CL}, and F_{CR} are the ocean-generated horizontal forces, F_{RL} and F_{RR} are the ridge push forces, F_{SP} is the slab pull force, F_{BA}, F_{AB}, F_{CB}, and F_{BC} are the collisional forces between three plates, f_A, f_B, and f_C are the basal friction forces exerted by the asthenosphere. According to Forsyth & Uyeda [22], if there is thermal convection in the asthenosphere, f_{base} would be a driving force [16] [17] [20] [21]. If, instead, the asthenosphere is passive relative to plate motion, f_{base} would be a resistive force. Clennett *et al.* [35] recently treated mantle flow as a resisting force opposite to plate motions. Here, we assume f_{base} to be a resistive force. Trench suction is neglected. It's worth noting that we now include slab pull in this model, which is intended to show that this force may be incorporated into our modelling of force balance. Each of these forces can yield a torque relative to the Earth's center, because torque is a product of force and lever arm, and therefore the lever arm may be represented with the Earth's radius since plate is too thin relative to the Earth's radius, the lever arm length of one plate may be approximately equal to that of another plate. This situation allows us to simplify the torque balance into the force balance for the discussion. We assume that Plate A and B rotate counterclockwise whereas Plate C rotates clockwise.

For Plate A, we set $F_{RL} = 4.0 \times 10^{12}$ N m^{-1}, this magnitude is widely accepted by geophysical community [31]. We assume the ocean depth to be 5.00 km at the right and 3.00 km at the left, respectively. This assumption is reasonable because the ocean depths around the world are various from one place to another. These two depths correspond to $F_{AR} = 0.1225 \times 10^{12}$ N m^{-1} and $F_{AL} = 0.0441 \times 10^{12}$ N m^{-1}, the final combined force of these two forces would be $F_{AR} - F_{AL} = 0.0784 \times 10^{12}$ N m^{-1}. We set $F_{BA} = 4.05 \times 10^{12}$ N m^{-1}, and use $F_{RL} = 4.0 \times 10^{12}$ N m^{-1} and a little

portion of the final combined force, which is represented by $F_{ARL} = 0.05 \times 10^{12}$ N m^{-1}, to balance out F_{BA}, and use the remaining final combined force $F_{RARL} = 0.0284 \times 10^{12}$ N m^{-1} to balance out the basal friction force f_A. The force balances for this plate would be $F_{BA} - F_{RL} - F_{ARL} = 0$ and $F_{RARL} - f_A = 0$.

For Plate B, which is an oceanic plate, we set $F_{CB} = 4.0 \times 10^{12}$ N m^{-1}, due to $F_{BA} = F_{AB} = 4.05 \times 10^{12}$ N m^{-1}, thus, $F_{AB} - F_{CB} = 0.05 \times 10^{12}$ N m^{-1}. We use this combined force and the net slab pull to balance out the basal friction force. As exhibited in Figure 7(c), the direction of the slab pull F_{SP} is tilt and downwards, this means that its contribution to the horizontal plate motion is largely discounted by the geometry of force. We here term the net slab pull that contributes to the horizontal plate motion as F_{NSP}. Schellart [63] estimated the net slab pull F_{NSP} to be at a magnitude of 4.1-6.1 $\times 10^{12}$ N m^{-1}. As a result, the force balance for this plate would be $F_{BA} - F_{CB} + F_{NSP} - f_B = 0$.

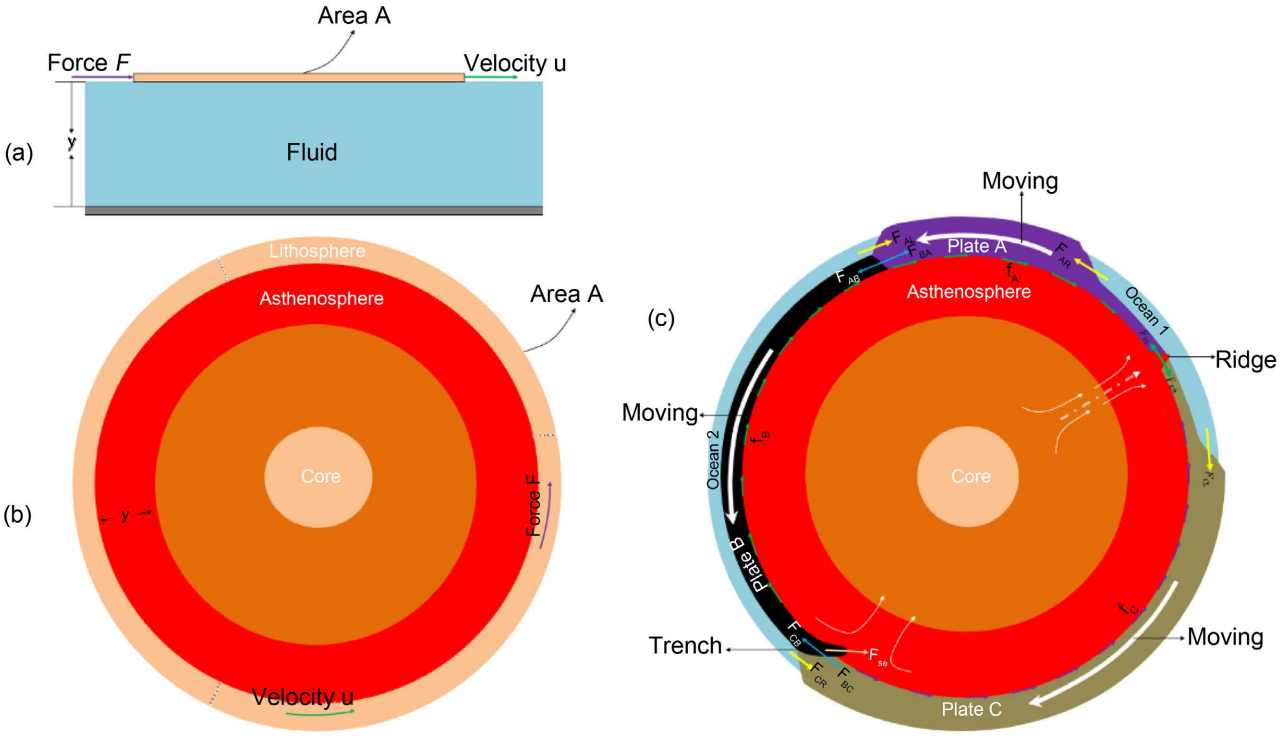

Figure 7. Conceptual model for the force balance of fluid mechanics. (a) A plate moving over a fluid. (b) The lithosphere moving over the asthenosphere. (c) The lithospheric plates moving over the underlying viscous asthenosphere.

For Plate C, we set $F_{RR} = 3.95 \times 10^{12}$ N m^{-1}, and assume the ocean depth to be 4 km at the left and 6 km at the right, respectively. These two depths correspond to $F_{CR} = 0.0784 \times 10^{12}$ N m^{-1} and $F_{CL} = 0.1764 \times 10^{12}$ N m^{-1}, the final combined force of these two forces would be F_{CL}-$F_{CR} = 0.098 \times 10^{12}$ N m^{-1}. Due to $F_{CB} = F_{BC} = 4.0 \times 10^{12}$ N m^{-1}, we use $F_{RR} = 3.95 \times 10^{12}$ Nm^{-1} and a little portion of the final combined force, which is represented by $F_{CLR} = 0.05 \times 10^{12}$ N m^{-1}, to balance out F_{BC}, and use the remaining final combined force $F_{RCLR} = 0.048 \times 10^{12}$ N m^{-1} to balance out the basal friction force f_C. The force balances for this plate would be $F_{BC} - F_{RR} - F_{CLR}$

= 0 and $F_{RCLR} - f_C = 0$.

These force balances allow three plates to be steadily rotated. We find, even if the ridge push force F_{RL} (F_{RR}) is given a smaller amplitude (~10^{10} N m^{-1}, for example), so long as the collisional force F_{BA} (F_{AB}, F_{CB}, and F_{BC}) is properly valued, these force balances can always be realized. Nevertheless, as demonstrated by Yang [33], a ridge push force of 4.0×10^{12} N m^{-1} would result in a horizontal stresses that are mostly concentrated on the lower part of the lithosphere, which is not agreement with the observed stresses that are mostly concentrated on the uppermost part of the lithosphere [64]-[66]. Hence, we prefer to accept the ridge push force to be smaller than ocean-generated force. Our demonstration reaches a point that irrespective of whether slab pull is included or not included, the force balance within our model remains consistently achievable.

3.2. How Does Plate Motion Realize Mechanically?

Thus far, we have concluded that ocean-generated force is able to combine the ridge push force, the collisional force, and the shearing force to satisfy the kinematics and geometry of plate motion. Now, let us address how plate motion can be mechanically realized. As shown in **Figure 7(c)**, it is assumed that the depth of Ocean 1 is greater than that of Ocean 2. If we use a part of Ocean 2 that connects to Plate A, which is equal in length to Ocean 1, to do comparison, the depth difference between this part of Ocean 2 and Ocean 1 creates a net gravitational potential energy relative to the asthenosphere reference level. As Plate A and Plate B move away from each other, this separation would require the Ocean 1 depth to decrease as the basin elongates horizontally, and require the Ocean 2 depth to increase as the basin shortens horizontally. Consequently, the net gravitational potential energy decreases. Therefore, if there were no external energy inputs to compensate, the net gravitational potential energy would eventually disappear, terminating plate motion. Tides may be supplying this energy. Tides represent the regular alternations of high and low water on Earth; when high water falls, the gravitational potential energy converts into kinetic energy, then, ocean water obtains movement. As all oceans are physically connected, part of the water in Ocean 2 may travel via passages to compensate the decreasing ocean depth of Ocean 1, thus sustaining the net gravitational potential energy. Given the basal friction force $f_{basal} = 1.62 \times 10^{18}$ N and the movement distance $u = 3$ cm/yr for the lithosphere, an energy of $Q_1 = f_{basal} \times u = 4.86 \times 10^{16}$ J/yr is required to satisfy this movement distance. This energy also represents the net gravitational potential energy. The ocean water level often increases twice a day due to tides, and the resultant height is assumed to be $h = 0.3$ m. Given the gravitational acceleration $g = 9.8$ m/s, the volume $v = 1.35 \times 10^9$ km^3 and density $\rho = 1000$ kg/m^3 for the whole ocean, and consequently, the gravitational potential energy obtained by ocean water due to tides during a year would be $Q_2 = 2 \times 365 \times \rho vgh = 2.9 \times 10^{21}$ J/yr. The transformation from gravitational potential energy to kinetic energy within ocean water and the energy transition between oceans must be complicated, and we

believe that a small part of this tidal energy is enough to supply the net gravitational potential energy. In fact, the impact of tidal energy on plate motion has long been discussed. Rochester [67] showed that the total energy released due to tidal friction exceeds 5×10^{19} ergs/s. Several authors [68] [69] concluded that the dissipation in both shallow seas and on the solid Earth is approximately 2×10^{19} ergs/s, and this amount of energy exceeds the lower bound set by seismic energy release by 2 orders of magnitude [70] and might be driving the plate motion. Other authors (e.g., [71] [72]) reevaluated the energy budget and found that the total energy released by tidal friction may reach up to 1.2×10^{20} J/yr, and approximately 0.8×10^{20} J/yr is dissipated in the oceans, shallow seas, and mantle, and the remaining energy is enough to maintain the lithosphere's rotation, estimated at approximately 1.27×10^{19} J/yr. In contrast to these studies, we provide another insight: the tidal energy obtained by ocean water may feed plate motion.

Our understanding of the impact of ocean on continent and lithospheric plate suggests that the ocean-generated force may have significantly contributed to the evolutions of continent and plate tectonics, but what's the detail of them?

Acknowledgements

We express sincere thanks to Jinmin Chen for conducting the vector force analysis and to Bernhard Steinberger, Jeroen van Hunen, Maureen D. Long, and Thorsten Becker for their helpful comments on earlier version of this research. No funding for this research.

Conflicts of Interest

The author declares no conflicts of interest regarding the publication of this paper.

References

[1] Wegener, A. (1915) The Origin of Continents and Oceans. Courier Dover Publications.

[2] Wegener, A. (1924) The Origin of Continents and Oceans (Entstehung der Kontinente und Ozeane). Methuen & Co.

[3] Hess, H.H. (1962) History of Ocean Basins. In: Engel, A.E.J., James, H.L. and Leonard, B.F., Eds., *Petrologic Studies*, Geological Society of America, 599-620. https://doi.org/10.1130/petrologic.1962.599

[4] Vine, F.J. and Matthews, D.H. (1963) Magnetic Anomalies over Oceanic Ridges. *Nature*, **199**, 947-949. https://doi.org/10.1038/199947a0

[5] Wilson, J.T. (1963) A Possible Origin of the Hawaiian Islands. *Canadian Journal of Physics*, **41**, 863-870. https://doi.org/10.1139/p63-094

[6] Raymond, C.A., Stock, J.M. and Cande, S.C. (2000) Fast Paleogene Motion of the Pacific Hotspots from Revised Global Plate Circuit Constraints. In: Richards, M.A., Gordon, R.G. and Van Der Hilst, R.D., Eds., *Geophysical Monograph Series*, American Geophysical Union, 359-375. https://doi.org/10.1029/gm121p0359

[7] Cande, S.C. and Kent, D.V. (1992) A New Geomagnetic Polarity Time Scale for the Late Cretaceous and Cenozoic. *Journal of Geophysical Research: Solid Earth*, **97**,

13917-13951. https://doi.org/10.1029/92jb01202

[8] Cande, S.C., LaBrecque, J.L., Larson, R.L., Pitman III, W.C., Golovchenko, X. and Haxby, W.F. (1989) Magnetic Lineations of the World's Ocean Basins. American Association of Petroleum Geologists.

[9] Ma, Z.J., Li, C.D. and Gao, X.L. (1996) General Characteristics of Global Tectonics in the Mesozoic and Cenozoic (in Chinese). *Geological Science and Technology Information*, **15**, 21-25.

[10] Wan, T.F. (1993) Tectonic Stress Field and Its Application to the Intraplate in Eastern China (in Chinese). Geological Publishing Company.

[11] Hibsch, C., Jarrige, J., Cushing, E.M. and Mercier, J. (1995) Palaeostress Analysis, a Contribution to the Understanding of Basin Tectonics and Geodynamic Evolution. Example of the Permian/Cenozoic Tectonics of Great Britain and Geodynamic Implications in Western Europe. *Tectonophysics*, **252**, 103-136. https://doi.org/10.1016/0040-1951(95)00100-x

[12] Wan, T.F. (2018) On the Dynamic Mechanics of Global Lithosphere Plate Tectonics (in Chinese). *Earth Science Frontiers*, **25**, 320-335.

[13] Hales, A.L. (1936) Convection Currents in the Earth. *Geophysical Journal International*, **3**, 372-379. https://doi.org/10.1111/j.1365-246x.1936.tb01744.x

[14] Holmes, A. (1931) Radioactivity and Earth Movements. *Nature*, **128**, 496-496. https://doi.org/10.1038/128496e0

[15] Pekeris, C.L. (1935) Thermal Convection in the Interior of the Earth. *Geophysical Journal International*, **3**, 343-367. https://doi.org/10.1111/j.1365-246x.1935.tb01742.x

[16] Runcorn, S.K. (1962) Towards a Theory of Continental Drift. *Nature*, **193**, 311-314. https://doi.org/10.1038/193311a0

[17] Runcorn, S.K. (1962) Convection Currents in the Earth's Mantle. *Nature*, **195**, 1248-1249. https://doi.org/10.1038/1951248a0

[18] McKenzie, D.P. (1968) The Influence of the Boundary Conditions and Rotation on Convection in the Earth's Mantle. *Geophysical Journal International*, **15**, 457-500. https://doi.org/10.1111/j.1365-246x.1968.tb00203.x

[19] McKenzie, D.P. (1969) Speculations on the Consequences and Causes of Plate Motions. *Geophysical Journal International*, **18**, 1-32. https://doi.org/10.1111/j.1365-246x.1969.tb00259.x

[20] Morgan, W.J. (1972) Deep Mantle Convection Plumes and Plate Motions. *AAPG Bulletin*, **56**, 203-213. https://doi.org/10.1306/819a3e50-16c5-11d7-8645000102c1865d

[21] Turcotte, D.L. and Oxburgh, E.R. (1972) Mantle Convection and the New Global Tectonics. *Annual Review of Fluid Mechanics*, **4**, 33-66. https://doi.org/10.1146/annurev.fl.04.010172.000341

[22] Forsyth, D. and Uyeda, S. (1975) On the Relative Importance of the Driving Forces of Plate Motion. *Geophysical Journal International*, **43**, 163-200. https://doi.org/10.1111/j.1365-246x.1975.tb00631.x

[23] Oxburgh, E.R. and Turcotte, D.L. (1978) Mechanisms of Continental Drift. *Reports on Progress in Physics*, **41**, 1249-1312. https://doi.org/10.1088/0034-4885/41/8/003

[24] Spence, W. (1987) Slab Pull and the Seismotectonics of Subducting Lithosphere. *Reviews of Geophysics*, **25**, 55-69. https://doi.org/10.1029/rg025i001p00055

[25] White, R. and McKenzie, D. (1989) Magmatism at Rift Zones: The Generation of Volcanic Continental Margins and Flood Basalts. *Journal of Geophysical Research*:

Solid Earth, **94**, 7685-7729. https://doi.org/10.1029/jb094ib06p07685

[26] Richardson, R.M. (1992) Ridge Forces, Absolute Plate Motions, and the Intraplate Stress Field. *Journal of Geophysical Research*: *Solid Earth*, **97**, 11739-11748. https://doi.org/10.1029/91jb00475

[27] Vigny, C., Ricard, Y. and Froidevaux, C. (1991) The Driving Mechanism of Plate Tectonics. *Tectonophysics*, **187**, 345-360. https://doi.org/10.1016/0040-1951(91)90474-7

[28] Bott, M.H.P. (1993) Modelling the Plate-Driving Mechanism. *Journal of the Geological Society*, **150**, 941-951. https://doi.org/10.1144/gsjgs.150.5.0941

[29] Tanimoto, T. and Lay, T. (2000) Mantle Dynamics and Seismic Tomography. *Proceedings of the National Academy of Sciences*, **97**, 12409-12410. https://doi.org/10.1073/pnas.210382197

[30] Conrad, C.P. and Lithgow-Bertelloni, C. (2002) How Mantle Slabs Drive Plate Tectonics. *Science*, **298**, 207-209. https://doi.org/10.1126/science.1074161

[31] Turcotte, D. and Schubert, G. (2014). Geodynamics. 3rd ed., Cambridge University Press. https://doi.org/10.1017/cbo9780511843877

[32] Cawood, P.A., Hawkesworth, C.J. and Dhuime, B. (2012) The Continental Record and the Generation of Continental Crust. *Geological Society of America Bulletin*, **125**, 14-32. https://doi.org/10.1130/b30722.1

[33] Yang, Y.F. (2024) The Dynamic Impact of Ocean on Continent. *International Journal of Geosciences*, **15**, 698-719. https://doi.org/10.4236/ijg.2024.159039

[34] Kanamori, H. (1994) Mechanics of Earthquakes. *Annual Review of Earth and Planetary Sciences*, **22**, 207-237. https://doi.org/10.1146/annurev.ea.22.050194.001231

[35] Clennett, E.J., Holt, A.F., Tetley, M.G., Becker, T.W. and Faccenna, C. (2023) Assessing Plate Reconstruction Models Using Plate Driving Force Consistency Tests. *Scientific Reports*, **13**, Article No. 10191. https://doi.org/10.1038/s41598-023-37117-w

[36] Cengel, Y.A. and Cimbala, J.M. (2017) Fluid Mechanics: Fundamentals and Applications. 4th Edition, McGraw-Hill Education.

[37] Kreemer, C., Blewitt, G. and Klein, E.C. (2014) A Geodetic Plate Motion and Global Strain Rate Model. *Geochemistry*, *Geophysics*, *Geosystems*, **15**, 3849-3889. https://doi.org/10.1002/2014gc005407

[38] Doglioni, C. and Panza, G. (2015) Polarized Plate Tectonics. *Advances in Geophysics*, **56**, 1-167. https://doi.org/10.1016/bs.agph.2014.12.001

[39] Faccincani, L., Faccini, B., Casetta, F., Mazzucchelli, M., Nestola, F. and Coltorti, M. (2021) EoS of Mantle Minerals Coupled with Composition and Thermal State of the Lithosphere: Inferring the Density Structure of Peridotitic Systems. *Lithos*, **404-405**, Article 106483. https://doi.org/10.1016/j.lithos.2021.106483

[40] Steinberger, B. (2016) Topography Caused by Mantle Density Variations: Observation-Based Estimates and Models Derived from Tomography and Lithosphere Thickness. *Geophysical Journal International*, **205**, 604-621. https://doi.org/10.1093/gji/ggw040

[41] Hager, B.H. and Richards, M.A. (1989) Long-Wavelength Variations in Earth's Geoid: Physical Models and Dynamical Implications. *Philosophical Transactions of the Royal Society of London*, *Series A*, **328**, 309-327.

[42] Mitrovica, J.X. (1996) Haskell [1935] Revisited. *Journal of Geophysical Research*: *Solid Earth*, **101**, 555-569. https://doi.org/10.1029/95jb03208

[43] King, S.D. (1995) The Viscosity Structure of the Mantle. *Reviews of Geophysics*, **33**,

11-17. https://doi.org/10.1029/95rg00279

[44] Kido, M., Yuen, D.A., Čadek, O. and Nakakuki, T. (1998) Mantle Viscosity Derived by Genetic Algorithm Using Oceanic Geoid and Seismic Tomography for Whole-Mantle versus Blocked-Flow Situations. *Physics of the Earth and Planetary Interiors*, **107**, 307-326. https://doi.org/10.1016/s0031-9201(98)00077-6

[45] James, T.S., Gowan, E.J., Wada, I. and Wang, K. (2009) Viscosity of the Asthenosphere from Glacial Isostatic Adjustment and Subduction Dynamics at the Northern Cascadia Subduction Zone, British Columbia, Canada. *Journal of Geophysical Research: Solid Earth*, **114**, B04405. https://doi.org/10.1029/2008jb006077

[46] Pollitz, F.F., Bürgmann, R. and Romanowicz, B. (1998) Viscosity of Oceanic Asthenosphere Inferred from Remote Triggering of Earthquakes. *Science*, **280**, 1245-1249. https://doi.org/10.1126/science.280.5367.1245

[47] Becker, T.W. (2017) Superweak Asthenosphere in Light of Upper Mantle Seismic Anisotropy. *Geochemistry, Geophysics, Geosystems*, **18**, 1986-2003. https://doi.org/10.1002/2017gc006886

[48] Kaufmann, G. and Lambeck, K. (2000) Mantle Dynamics, Postglacial Rebound and the Radial Viscosity Profile. *Physics of the Earth and Planetary Interiors*, **121**, 301-324. https://doi.org/10.1016/s0031-9201(00)00174-6

[49] Hu, Y., Bürgmann, R., Banerjee, P., Feng, L., Hill, E.M., Ito, T., *et al.* (2016) Asthenosphere Rheology Inferred from Observations of the 2012 Indian Ocean Earthquake. *Nature*, **538**, 368-372. https://doi.org/10.1038/nature19787

[50] Bercovici, D., Tackley, P.J. and Ricard, Y. (2015) The Generation of Plate Tectonics from Mantle Dynamics. In: Schubert, G., Ed., *Treatise on Geophysics*, Elsevier, 271-318. https://doi.org/10.1016/b978-0-444-53802-4.00135-4

[51] Mei, S., Bai, W., Hiraga, T. and Kohlstedt, D.L. (2002) Influence of Melt on the Creep Behavior of Olivine-Basalt Aggregates under Hydrous Conditions. *Earth and Planetary Science Letters*, **201**, 491-507. https://doi.org/10.1016/s0012-821x(02)00745-8

[52] Hirth, G. and Kohlstedt, D.L. (1996) Water in the Oceanic Upper Mantle: Implications for Rheology, Melt Extraction and the Evolution of the Lithosphere. *Earth and Planetary Science Letters*, **144**, 93-108. https://doi.org/10.1016/0012-821x(96)00154-9

[53] Doglioni, C., Ismail-Zadeh, A., Panza, G. and Riguzzi, F. (2011) Lithosphere-Asthenosphere Viscosity Contrast and Decoupling. *Physics of the Earth and Planetary Interiors*, **189**, 1-8. https://doi.org/10.1016/j.pepi.2011.09.006

[54] Scoppola, B., Boccaletti, D., Bevis, M., Carminati, E. and Doglioni, C. (2006) The Westward Drift of the Lithosphere: A Rotational Drag? *Geological Society of America Bulletin*, **118**, 199-209. https://doi.org/10.1130/b25734.1

[55] Korenaga, J. and Karato, S. (2008) A New Analysis of Experimental Data on Olivine Rheology. *Journal of Geophysical Research: Solid Earth*, **113**, B02403. https://doi.org/10.1029/2007jb005100

[56] Kawakatsu, H., Kumar, P., Takei, Y., Shinohara, M., Kanazawa, T., Araki, E., *et al.* (2009) Seismic Evidence for Sharp Lithosphere-Asthenosphere Boundaries of Oceanic Plates. *Science*, **324**, 499-502. https://doi.org/10.1126/science.1169499

[57] Hawley, W.B., Allen, R.M. and Richards, M.A. (2016) Tomography Reveals Buoyant Asthenosphere Accumulating beneath the Juan De Fuca Plate. *Science*, **353**, 1406-1408. https://doi.org/10.1126/science.aad8104

[58] Holtzman, B.K. (2016) Questions on the Existence, Persistence, and Mechanical Effects of a Very Small Melt Fraction in the Asthenosphere. *Geochemistry, Geophysics,*

Geosystems, **17**, 470-484. https://doi.org/10.1002/2015gc006102

[59] Naif, S., Key, K., Constable, S. and Evans, R.L. (2013) Melt-Rich Channel Observed at the Lithosphere-Asthenosphere Boundary. *Nature*, **495**, 356-359. https://doi.org/10.1038/nature11939

[60] Freed, A.M., Hashima, A., Becker, T.W., Okaya, D.A., Sato, H. and Hatanaka, Y. (2017) Resolving Depth-Dependent Subduction Zone Viscosity and Afterslip from Postseismic Displacements Following the 2011 Tohoku-Oki, Japan Earthquake. *Earth and Planetary Science Letters*, **459**, 279-290. https://doi.org/10.1016/j.epsl.2016.11.040

[61] Stern, T.A., Henrys, S.A., Okaya, D., Louie, J.N., Savage, M.K., Lamb, S., *et al.* (2015) A Seismic Reflection Image for the Base of a Tectonic Plate. *Nature*, **518**, 85-88. https://doi.org/10.1038/nature14146

[62] Jordan, T.H. (1974) Some Comments on Tidal Drag as a Mechanism for Driving Plate Motions. *Journal of Geophysical Research*, **79**, 2141-2142. https://doi.org/10.1029/jb079i014p02141

[63] Schellart, W.P. (2004) Quantifying the Net Slab Pull Force as a Driving Mechanism for Plate Tectonics. *Geophysical Research Letters*, **31**, L07611. https://doi.org/10.1029/2004gl019528

[64] Zoback, M.L., Zoback, M.D., Adams, J., Assumpção, M., Bell, S., Bergman, E.A., *et al.* (1989) Global Patterns of Tectonic Stress. *Nature*, **341**, 291-298. https://doi.org/10.1038/341291a0

[65] Zoback, M.L. and Magee, M. (1991) Stress Magnitudes in the Crust: Constraints from Stress Orientation and Relative Magnitude Data. *Philosophical Transactions of the Royal Society*, **A337**, 181-194.

[66] Zoback, M.L. (1992) First- and Second-Order Patterns of Stress in the Lithosphere: The World Stress Map Project. *Journal of Geophysical Research*: *Solid Earth*, **97**, 11703-11728. https://doi.org/10.1029/92jb00132

[67] Rochester, M.G. (1973) The Earth's Rotation. *Eos*, *Transactions American Geophysical Union*, **54**, 769-780. https://doi.org/10.1029/eo054i008p00769

[68] Miller, G.R. (1966) The Flux of Tidal Energy Out of the Deep Oceans. *Journal of Geophysical Research*, **71**, 2485-2489. https://doi.org/10.1029/jz071i010p02485

[69] Munk, W. (1968) Once Again-Tidal Friction. *Quarterly Journal of the Royal Astronomical Society*, **9**, 352-375.

[70] Gutenberg, B. (1956) The Energy of Earthquakes. *Quarterly Journal of the Geological Society of London*, **112**, 1-14. https://doi.org/10.1144/gsl.jgs.1956.112.01-04.02

[71] Riguzzi, F., Panza, G., Varga, P. and Doglioni, C. (2010) Can Earth's Rotation and Tidal Despinning Drive Plate Tectonics? *Tectonophysics*, **484**, 60-73. https://doi.org/10.1016/j.tecto.2009.06.012

[72] Egbert, G.D. and Ray, R.D. (2000) Significant Dissipation of Tidal Energy in the Deep Ocean Inferred from Satellite Altimeter Data. *Nature*, **405**, 775-778. https://doi.org/10.1038/35015531